International Journal of Geosciences, 2025, 16(10), 701-721
https://www.scirp.org/journal/ijg
ISSN Online: 2156-8367
ISSN Print: 2156-8359

Petrogenesis and Tectonic Significance of Meta-Mafic Rocks from Eastern Mayo Kebbi Massif (Pala), Chad: Evidence for a Depleted Mantle Source and Intra-Oceanic Subduction

Félix Nenadji Djerossem[1*], Gustave Ronang Baïssemia[2], Moussa Ngarena Klamadji[2], Mbaguedje Diondoh[3]

[1]Department of Mining, New and Renewable Energies. National Higher Institute of the Sahara and Sahel, Iriba, Chad
[2]Department of Mining and Geological Engineering, Faculty of Life and Earth Sciences, Pala University, Pala, Chad
[3]Department of Geology, Faculty of Sciences and Techniques, University Adam Barka of Abeché, Abeché, Chad
Email: *Djerossem@gmail.com

How to cite this paper: Djerossem, F.N., Baïssemia, G.R., Klamadji, M.N. and Diondoh, M. (2025) Petrogenesis and Tectonic Significance of Meta-Mafic Rocks from Eastern Mayo Kebbi Massif (Pala), Chad: Evidence for a Depleted Mantle Source and Intra-Oceanic Subduction. *International Journal of Geosciences*, **16**, 701-721.
https://doi.org/10.4236/ijg.2025.1610035

Received: September 8, 2025
Accepted: October 26, 2025
Published: October 29, 2025

Abstract

Meta-mafic rocks from the eastern Mayo Kebbi massif (Pala area, Chad) provide new insights into the geodynamic evolution of the Central African Orogenic Belt (CAOB). Petrographic and geochemical analyses reveal that the meta-mafic rocks consist of amphibolites and métagabbros, derived from a basalts protolith. These rocks exhibit calc-alkaline to tholeiitic affinities and are characterized by granoblastic and microlitic porphyritic textures. Enrichment in light rare earth elements (LREE), parallel REE patterns, and systematic variations in major and trace elements indicate that fractional crystallization was the dominant differentiation process. These rocks formed in a primitive arc magmatic setting, with source components including N-MORB-type and depleted mantle. Discrimination diagrams (e.g., V/Ti vs. Zr, Th/Yb vs. Nb/Yb) indicate an intra-oceanic subduction influence, supported by negative anomalies in Nb-Ta, Zr-Hf and Ti. These findings support a tectonic model involving an active margin between a mid-ocean ridge and an intra-oceanic arc, reflecting the closure or subduction of an ancient oceanic domain.

Keywords

Meta-Mafic Rocks, Mayo Kebbi, N-MORB, Depleted Mantle, Central African Orogenic Belt

1. Introduction

The Mayo Kebbi orogenic belt forms part of the Central African Orogenic Belt

(CAOB), which was reactivated during the Pan-African orogeny between 700 and 500 Ma [1] [2]. The CAOB is located between the Congo Craton and the Saharan metacraton (**Figure 1**), and was formed through the convergence of the West African and Congo-São Francisco cratons, along with the Saharan metacraton, during the assembly of Western Gondwana [3] [4]. This belt is geologically correlated with the Borborema Province in northeastern Brazil, which also belongs to the Neoproterozoic Brasiliano Orogenic System [5]-[11]. Numerous studies focusing on tectonic evolution and associated magmatic activity have led to the interpretation of a continent-continent collision within the CAOB [12]-[16].

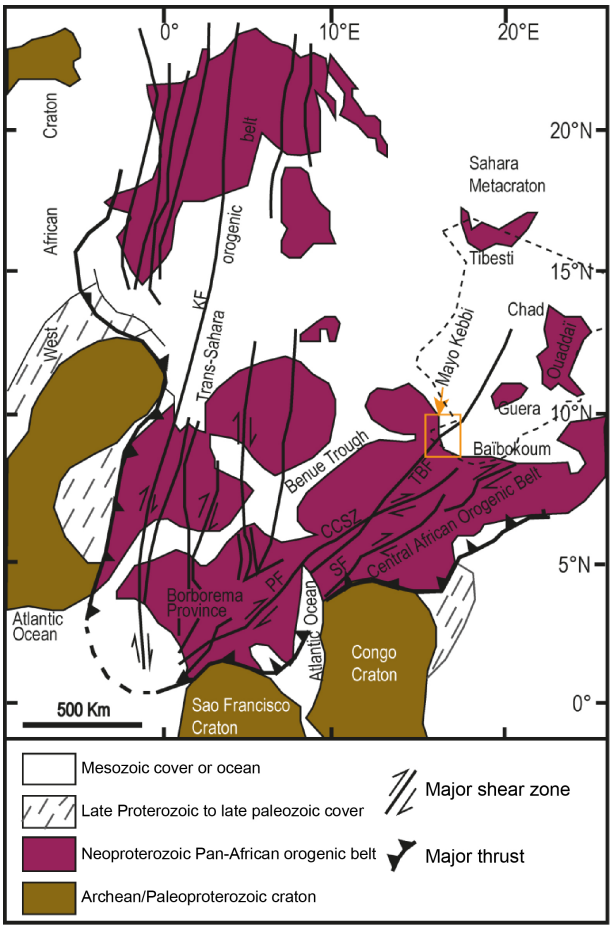

Figure 1. Geological sketch map of west-central Africa and northern Brazil with cratonic masses and the Pan-African/Brasiliano provinces of the Pan-Gondwana belt in a Pangea reconstruction [3] [4]. TBF: Tcholliré-Banyo fault, CCSZ: Central Cameroon shear zone, PF: Pernambuco fault, SF: Sanaga fault, KF: Kandi fault. Dashed outline roughly marks the political boundary of Chad.

In Chad, the Central African Orogenic Belt comprises Precambrian formations subdivided into five principal massifs: (1) The Tibesti Massif (North), characterized by Pan-African granitic crust [17] [18] overlying Paleoproterozoic metamorphic units dominated by metasedimentary formations [19]-[21]. (2) The Ouaddaï

Massif (East), composed of (a) Archean to Paleoproterozoic crust reworked during the Pan-African orogeny, and (b) juvenile Neoproterozoic crust [22]-[26]. (3) The Guéra Massif (Central Chad) consists of Neoproterozoic crust dominated by Pan-African calc-alkaline granites [27] [28]. (4) The Baïbokoum Massif (Far South), exposes Neoproterozoic crust composed of calc-alkaline granites with enclaves of metasedimentary and amphibolitic rocks [29]-[31]. (5) The Mayo Kebbi Massif (Southwest), defined by juvenile Neoproterozoic crust, comprising from bottom to top: (a) mafic to ultramafic plutonic complexes, (b) greenstone belts of metasedimentary and metavolcanic rocks, and (c) various calc-alkaline granites emplaced in an intra-oceanic arc setting during successive extensional and compressional phases [21] [32] [33]. Despite extensive studies in the western part of the Mayo Kebbi Massif (Léré), the meta-mafic rocks of the eastern sector (Pala) remain poorly characterized in terms of geochemistry. The origin of their sources and associated tectonic environments has not yet been clearly established.

In this paper, we present petrographic and geochemical data (major elements, trace elements, and rare earth elements) of the meta-mafic rocks from the eastern Mayo Kebbi Massif (Pala), with the aim of elucidating their origin and constraining their tectonic setting.

2. Geological Setting of the Mayo Kebbi Massif

The Mayo Kebbi Massif corresponds to the northeastern extension of the Poli region in northern Cameroon [21] [34] (**Figure 1**, **Figure 2**). It is predominantly composed of juvenile Neoproterozoic crust, consisting of granitic bodies and greenstone belts [31] [33] [34]-[36]. The greenstone belts are represented by the Zalbi Series in the west and the Goueygoudoum Series in the east. The Zalbi Series forms an elongated basin trending SSW-NNE [37], and comprises metagabbros, metabasalts, chlorite schists, talc schists, and serpentinites [31] [32] [37]. The Goueygoudoum Series is poorly exposed and consists of metabasalts associated with metacarbonatites and metacherts. The felsic to mafic metavolcanic rocks of both series exhibits a tholeiitic geochemical signature, suggesting their development within an island arc and/or back-arc basin setting [31].

The batholiths of the Mayo Kebbi Massif are mainly composed of tonalites, diorites, granodiorites, and granites, which contain large xenoliths of polydeformed banded amphibolites [34]. These batholiths, represented by syn- to post-tectonic tonalites, intrude the Zalbi and Goueygoudoum Series [34] [36]. The post-tectonic granitoids include granodiorites, monzodiorites from Pala, and uraniferous granites from Zalbi [34]. The Zalbi granitic pluton comprises coarse-grained biotite-hornblende granite and fine-grained granite [33]. Petrographic and geochemical data indicate that this pluton consists of A-type granites crystallized from highly evolved magmas [33]. U-Pb zircon geochronological data reveal a crystallization age of 567 ± 10 Ma, with older xenocrystic Neoproterozoic zircons dated at 667 ± 5 Ma [33]. The coarse-grained biotite-hornblende granites are characterized by εNd values (εNd = +7.4) indicative of a depleted mantle source at 570 Ma [3].

Based on geochronological, geochemical, and Nd isotopic data, [33] proposed the following model for the origin of the Zalbi granitic pluton: (a) Contribution from juvenile magmas or partial melting of a juvenile basaltic protolith with a short crustal residence time; (b) Interaction of granitic magmas with older continental materials; (c) Fractional crystallization of biotite-bearing granite and (d) Crystallization of feldspars and ferromagnesian minerals.

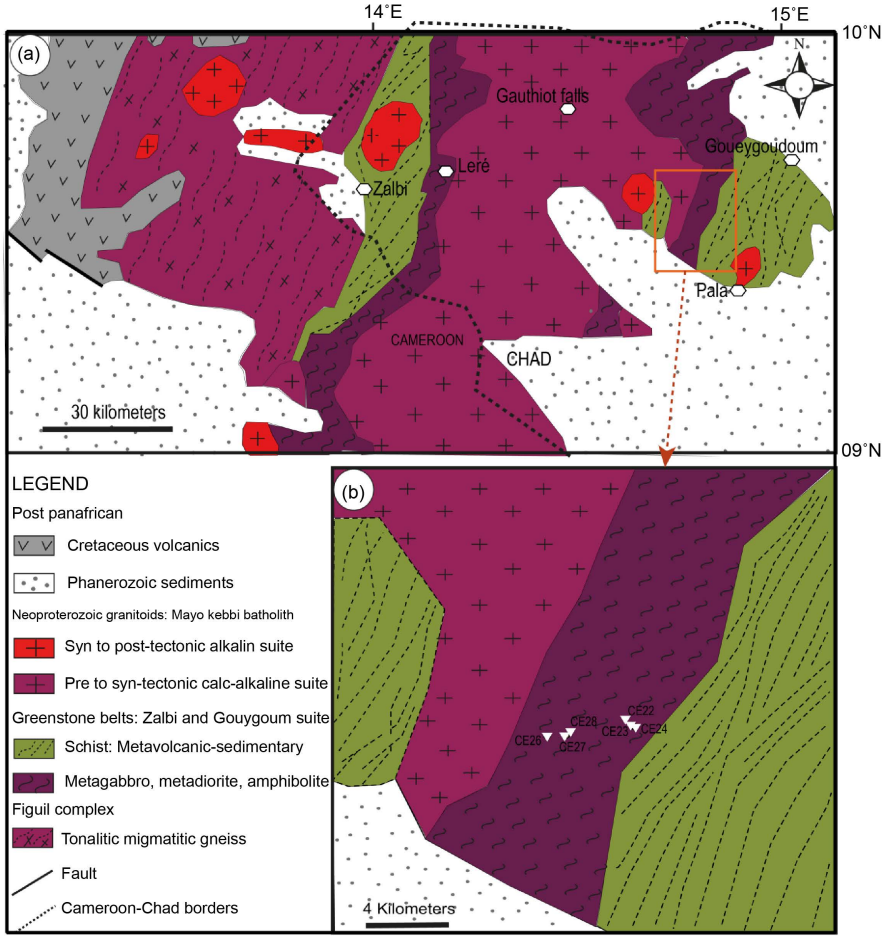

Figure 2. (a) Geological sketch map of the Mayo Kebbi and neighbouring regions. (b) map of the study area with the position of the samples to be used in the geochemical study.

3. Analytical Methods

Rock samples were sawed into chips for thin section preparation and trimmed to small blocks for geochemical investigations. About 200 to 500 g of each sample was crushed into a steel jaw crusher and then pulverized with an agate ball mill. Powders were digested using an alkali fusion procedure where the powder was mixed to lithium metaborate and melted to produce a glass pellet. The pellet was digested into diluted nitric acid before analyses. Analyses and digestions were made at the ALS Geochemistry-Loughrea (Ireland). Prepared samples (0.100 g) are added to lithium metaborate/lithium tetraborate flux, mixed well and fused in

a furnace at 1000˚C. The resulting melt is then cooled and dissolved in 100 mL of 4% nitric acid/2% hydrochloric acid. This solution is then analysed by ICP-AES and the results are corrected for spectral inter-element interferences. Oxide concentration is calculated from the determined elemental concentration and the result is reported in that format. The Whole Rock analysis is determined in conjunction with a loss-on-ignition at 1000˚C. The resulting data from both determinations are combined to produce a "total". For the determination of trace-elements, the samples were mixed well and fused in a furnace at 1025˚C. The resulting melt is then cooled and dissolved in an acid mixture containing nitric, hydrochloric and hydrofluoric acids. This solution is then analyzed by ICP-MS.

4. Petrography

4.1. Amphibolite

The amphibolites occur as massive or banded outcrops (Figure 3(a)), typically forming large blocks. They exhibit light to dark green coloration and are predominantly composed of ferromagnesian minerals. Under the microscope, the amphibolites display a granoblastic texture, characterized by abundant porphyroblasts of amphibole (Figure 3(b)), along with plagioclase, alkali feldspar, quartz,

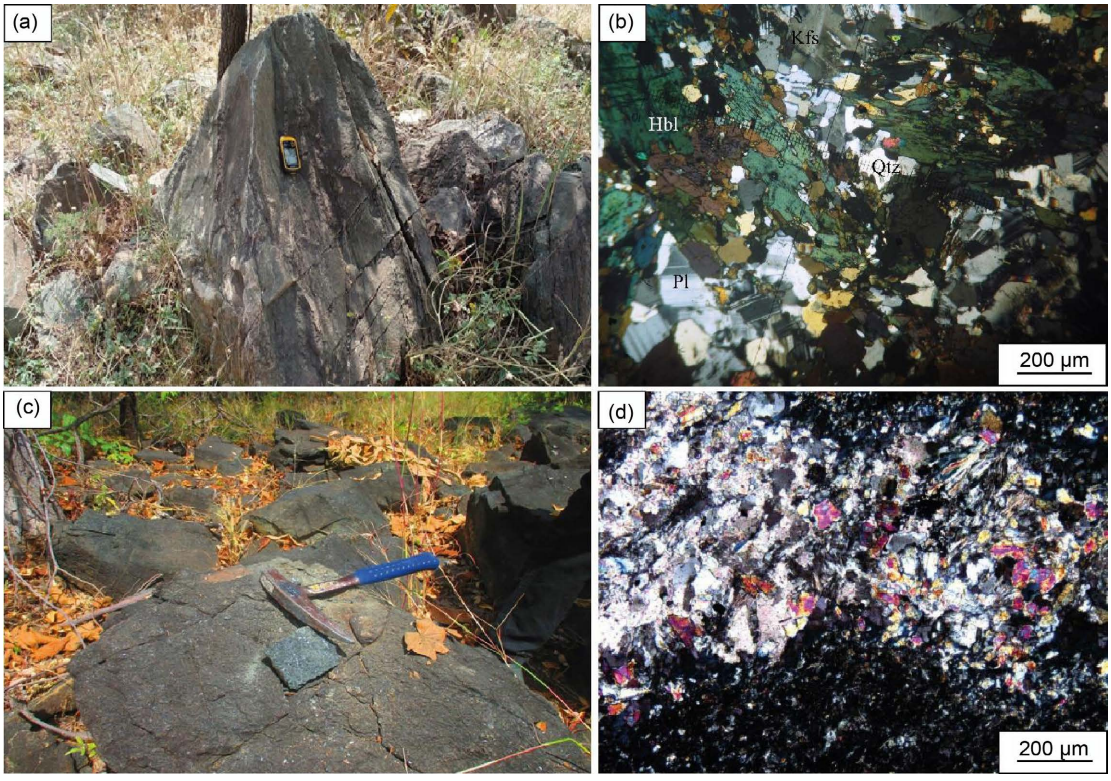

Figure 3. Field and microscopic views of amphibolites and metabasalts: (a) Outcrop morphology of amphibolites: massive or banded blocks with greenish coloration; (b) Photomicrograph of amphibolites: granoblastic texture dominated by porphyroblasts of amphibole; (c) Outcrop morphology of metabasalts: dark-colored blocks with diffuse lithological contacts; (d) Photomicrograph of metabasalts: microlitic porphyritic texture with actinolite, biotite, feldspar, and quartz.

biotite, apatite, sphene, zircon, and iron oxides. Amphibole (30% - 40%) is euhedral to subhedral and shows oblique extinction typical of green hornblende. It contains inclusions of apatite and opaque minerals. Plagioclase (18% - 25%) is also euhedral to subhedral, with inclusions of amphibole, apatite, and opaques, and shows initial signs of damouritization. Pyroxene (10% - 15%) is euhedral to subhedral, marked by double cleavage and inclusions of apatite and opaques. It also appears as granules between amphibole crystals and often exhibits myrmekitic texture with undulatory extinction.

Alkali feldspar (5% - 8%) occurs as large subhedral grains associated with quartz and amphibole, and contains apatite inclusions. Biotite (3% - 5%) is somewhat elongated and occupies interstitial spaces within the amphibolite. Quartz (2% - 3%) is anhedral with slightly lobate margins and sinuous contacts with amphibole. Apatite (<2%) appears as hexagonal sections, often included within feldspars and amphibole, with crystals that are rounded or elongated. Sphene (<2%) is euhedral to subhedral, commonly associated with plagioclase, and may contain opaque inclusions. Zircon (<1%) is observed as inclusions within amphibole and biotite.

4.2. Metabasalts

The metabasalts crop out as dark-colored blocks (**Figure 3(c)**), with diffuse contacts between them and adjacent lithologies. Microscopically, the metabasalts (**Figure 3(d)**) exhibit a microlitic porphyritic texture. The microlites consist of feldspar, albite, biotite, chlorite, and quartz. Diffuse patches of leucoxene are present, likely derived from the alteration of magmatic iron and/or titanium oxides. These are associated with green chlorite zones, sometimes accompanied by actinolite, carbonate clusters, and quartz. The groundmass contains rare prismatic feldspar crystals with polysynthetic twinning, alongside numerous actinolite prisms and partially chloritized biotite. Subhedral plagioclase microlites, somewhat stubby in shape, are transformed into albite, sericite, chlorite, quartz, and occasionally calcite.

5. Geochemistry

5.1. Classification

Geochemical data (major, trace and rare earth elements) obtained from six representative samples are presented in **Table 1**. In the total alkali versus silica (TAS) diagram [38], the amphibolite samples plot within the basanite, basalt, and andesite fields, while the metagabbro samples fall predominantly within the basalt field (**Figure 4(a)**). This classification, based on Na_2O and K_2O contents, remains debatable due to the potential mobility of these elements during intrusive processes.

According to [38], the Zr/Ti vs Nb/Y diagram (**Figure 4(b)**) is more reliable, as it utilizes immobile elements during greenschist facies metamorphism. In this diagram, both amphibolites and metagabbros cluster within the basalt field, suggesting that these rocks may have originated from a common parental magma.

Table 1. Major, trace and rare earth elements concentration data of amphibolites and metagabbros samples from Eastern part of Mayo Kebbi (Pala).

Rock type	Amphibolite			Métagabbro		
Samples	CE22	CE23	CE26	CE24	CE27	CE28
SiO_2	44.10	59.80	51.40	50.70	49.10	47.20
Al_2O_3	16.25	16.35	16.25	14.05	7.21	15.40
Fe_2O_3	8.49	6.09	8.58	8.62	10.10	7.90
MgO	6.79	4.95	9.38	9.53	17.15	12.45
CaO	8.94	5.20	8.96	8.04	11.75	12.20
Na_2O	2.82	3.89	2.68	2.63	1.31	1.37
K_2O	0.80	0.90	0.17	1.44	0.20	0.16
TiO_2	0.83	0.61	0.33	0.83	0.78	0.44
P_2O_5	0.15	0.13	0.04	0.13	0.03	0.01
MnO	0.13	0.12	0.13	0.14	0.18	0.13
Cr_2O_3	0.03	0.01	0.05	0.07	0.08	0.06
LOI	10.40	1.95	2.20	2.36	0.98	2.19
Total	99.73	100.00	100.17	98.54	98.87	99.51
Mg#	61.30	61.70	68.40	68.70	77.10	75.70
FeOt	7.65	5.59	7.73	7.77	9.10	7.12
Sc	27.40	19.60	29.80	37.40	62.90	38.80
V	210.00	84.00	117.00	227.00	216.00	128.00
Co	31.00	7.00	37.00	42.00	65.00	53.00
Ni	92.00	1.00	151.00	190.00	309.00	140.00
Cr	176.00	96.00	331.00	483.00	576.00	390.00
Cu	97.00	12.00	4.00	37.00	48.00	87.00
Zn	86.00	80.00	74.00	94.00	80.00	56.00
Rb	13.20	12.80	1.10	22.60	0.50	0.90
Sr	592.00	516.00	693.00	345.00	184.50	557.00
Ba	219.00	369.00	72.70	339.00	53.30	64.00
La	4.60	4.10	3.00	7.40	3.70	1.80
Ce	12.40	10.20	7.00	17.20	11.80	4.90
Pr	1.97	1.56	1.02	2.95	1.95	0.81
Nd	9.60	7.70	5.00	14.40	10.80	4.20
Sm	2.57	2.21	1.45	3.40	3.13	1.45
Eu	0.98	0.94	0.60	1.12	0.84	0.55
Gd	2.97	2.85	1.48	3.47	3.08	1.56
Tb	0.46	0.52	0.26	0.53	0.55	0.25
Dy	2.71	3.44	1.48	2.96	3.04	1.62

Continued

Ho	0.53	0.71	0.31	0.62	0.64	0.31
Er	1.45	2.15	0.82	1.74	1.85	0.91
Tm	0.22	0.33	0.13	0.26	0.26	0.12
Yb	1.42	2.13	0.77	1.52	1.54	0.72
Lu	0.24	0.31	0.14	0.23	0.22	0.11
Y	14.30	20.20	7.90	18.40	17.20	8.00
Zr	54.00	54.00	16.00	42.00	39.00	19.00
Hf	1.62	1.64	0.57	1.53	1.41	0.72
Ta	0.10	0.20	0.10	0.30	0.20	0.10
Pb	11.00	5.00	7.00	7.00	4.00	6.00
Th	0.06	0.42	0.09	0.19	0.06	0.09
U	0.12	0.18	<0.05	0.16	<0.05	<0.05

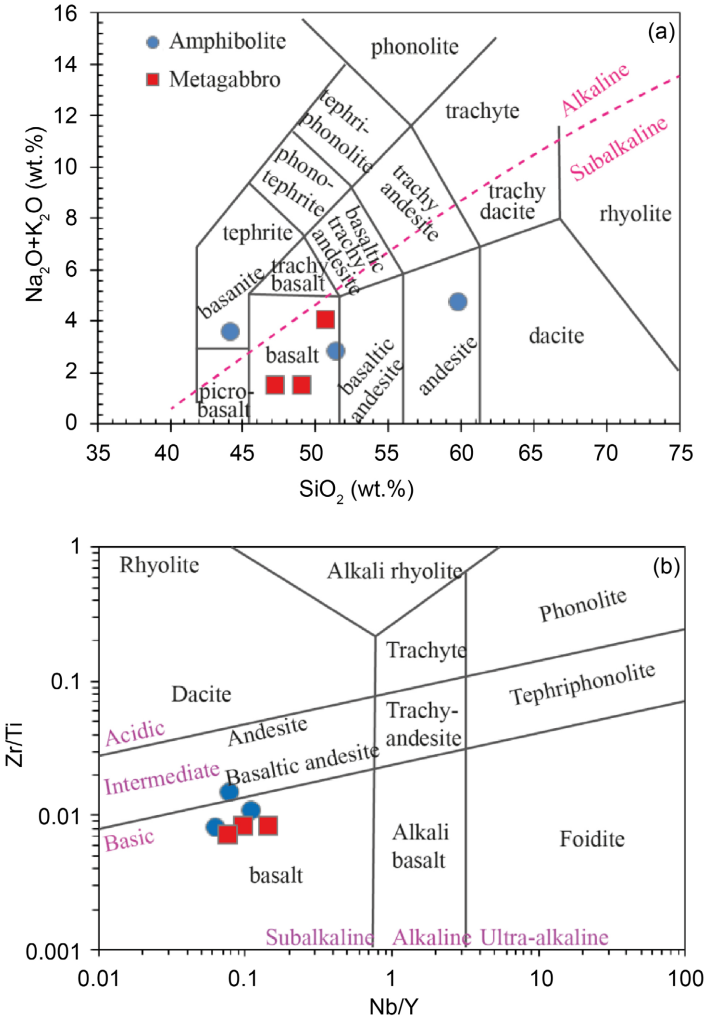

Figure 4. Classification diagrams: (a) Total alkali vs. silica diagram [39]. Alkaline-Tholeiite line from [40]. (b) Zr/Ti vs. Nb/Yb diagram [40].

In the AFM ternary diagram (Figure 5(a)), amphibolites and metagabbros exhibit a calc-alkaline trend. All metagabbro samples are classified as magnesian in the YCT triangular diagram (Y+Zr-Cr-TiO_2 × 100; Figure 5(b)). Amphibolite samples are distributed across alkaline, tholeiitic, and magnesian trends.

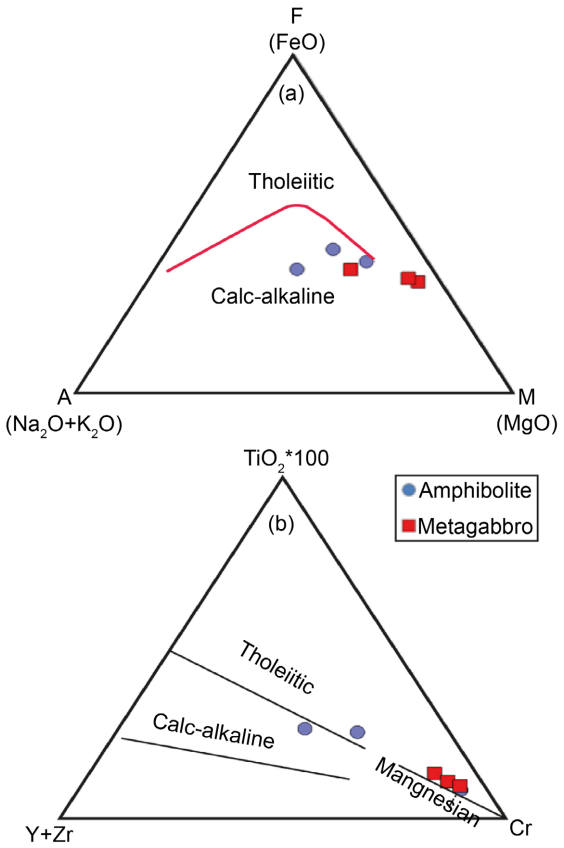

Figure 5. (a) AFM [40] and (b) YTC [41] plots of amphibolites and métagabbros.

5.2. Major Elements

The three amphibolite samples are characterized by SiO_2 contents ranging from 44.1 to 59.8 wt.%. Fe_2O_3 (6.09 - 8.58 wt.%), Al_2O_3 (16.25 - 16.35 wt.%), and CaO (5.2 - 8.96 wt.%) concentrations are moderate to high. The Mg number values (Mg# = 61.3 - 68.7) and MgO contents (4.95 - 9.38 wt.%) are highly variable, while the total alkali content (Na_2O + K_2O) ranges from 2.85 to 4.79 wt.%.

Metagabbros exhibit slightly lower SiO_2 contents (47.2 - 50.7 wt.%) compared to amphibolites. Their Fe_2O_3 (7.9 - 10.1 wt.%), Al_2O_3 (7.21 - 15.4 wt.%), and CaO (8.04 - 12.2 wt.%) contents are broadly similar to those of the amphibolites. However, they are distinguished by higher MgO concentrations (9.53 - 17.15 wt.%) and more variable Mg number values (Mg# = 68.7 - 77.1).

Binary diagrams plotted against MgO (Figure 6) reveal positive correlations with Fe_2O_3, MnO, and CaO, and negative correlations with Al_2O_3, Na_2O, K_2O, and

SiO_2. The samples show scattered distributions with respect to TiO_2.

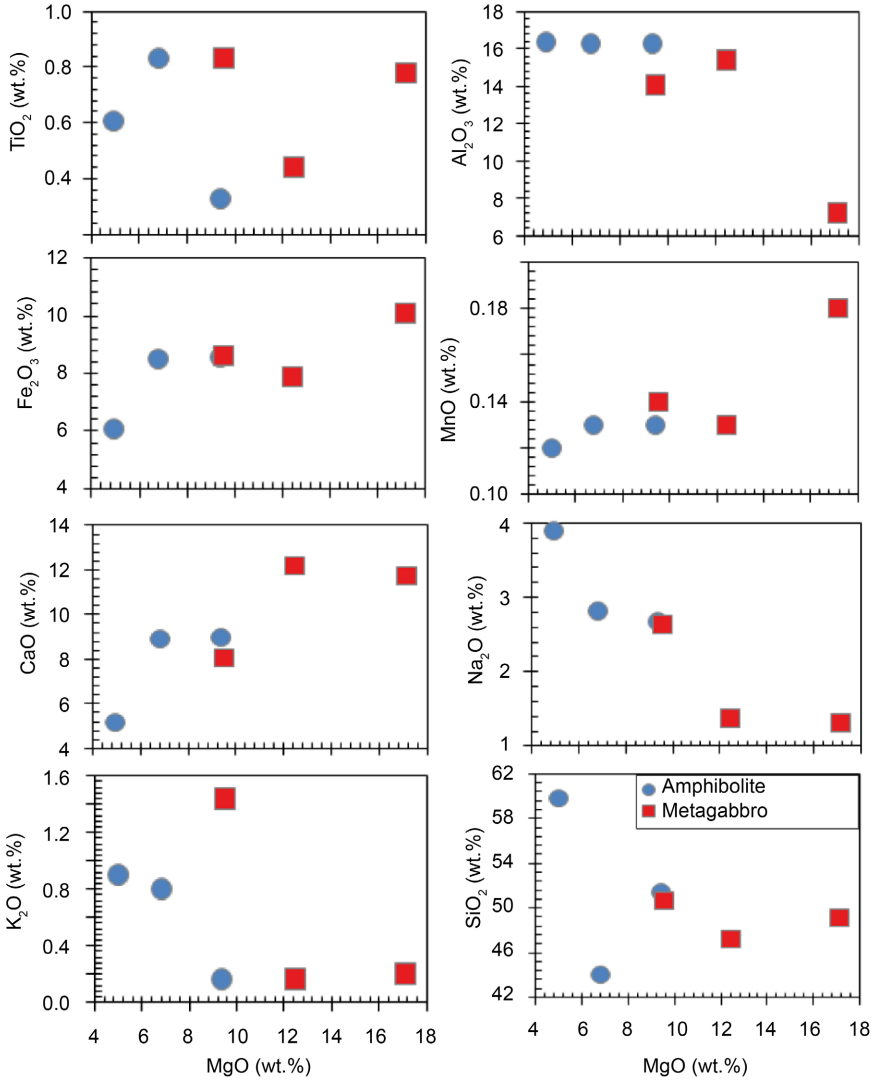

Figure 6. Major element variation diagrams of the amphibolites and métagabbros samples in terms of MgO.

5.3. Trace Elements

Amphibolites display relatively low to moderate concentrations of Ni (1 - 151 ppm), Cr (96 - 331 ppm), and V (84 - 210 ppm). Large-ion lithophile elements (LILEs) such as Ba and Sr vary between 72.7 - 369 ppm and 516 - 693 ppm, respectively. In the chondrite-normalized rare earth element (REE) diagram (**Figure 8(a)**), amphibolites exhibit subparallel spectra with slight enrichment in light REEs (LREEs) $((La/Yb)_n = 1.38 - 2.79)$ relative to middle and heavy REEs $((Gd/Yb)_n = 1.10 - 1.73)$. These rocks also show a weak positive Eu anomaly $((La/Sm)_n = 1.15 - 1.33)$.

Binary diagrams plotted against MgO reveal positive trends for V, Co, Cr, and Ni, and negative trends for Ba and Zr (**Figure 7**). In the primitive mantle-normal-

ized spider diagram (Figure 8(b)), amphibolites show enrichment in LILEs such as Ba, K, and Sr, along with negative anomalies in Nb-Ta and Zr-Hf, suggesting a subduction-related signature. All amphibolite samples are marked by strong positive Pb anomalies.

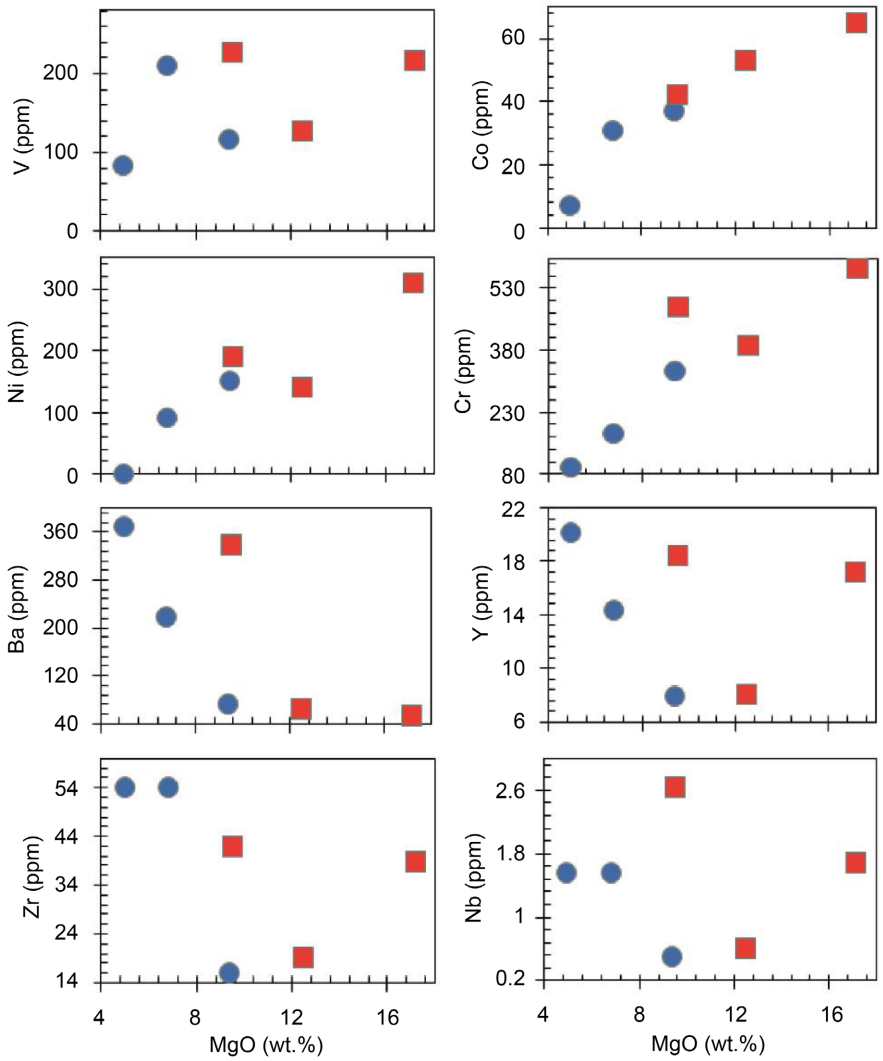

Figure 7. Trace element variation diagrams of the amphibolites and métagabbros samples in terms of MgO.

Metagabbros display relatively high concentrations of Ni (140 - 309 ppm), Cr (390 - 576 ppm), and V (128 - 227 ppm) compared to amphibolites. Ba and Sr contents range from 64 to 339 ppm. In the chondrite-normalized REE diagram (Figure 8(a)), metagabbros exhibit slight LREE enrichment ($(La/Yb)_n$ = 1.72 - 3.49) relative to MREE and HREE ($(Gd/Yb)_n$ = 1.64 - 1.88), with weak positive and negative Eu anomalies ($(La/Sm)_n$ = 0.76 - 1.40). Their REE spectra are subparallel to those of island arc basalts (IAB).

In the primitive mantle-normalized spider diagram (Figure 8(b)), metagabbros show enrichment in LILEs (Ba, K, Sr) relative to high field strength elements

(HFSEs) such as Nb, Zr, Hf, and Ti. Notable negative anomalies are observed in Th and Pr.

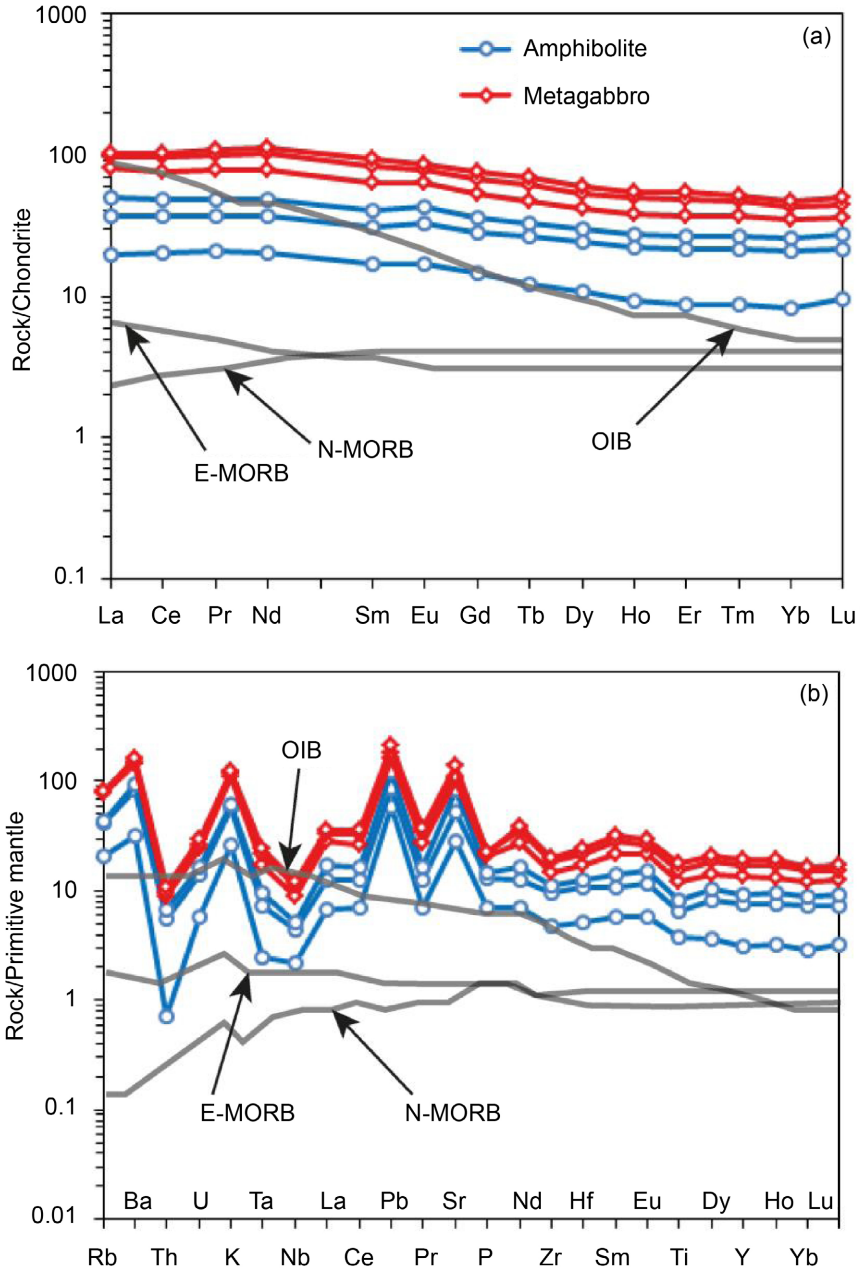

Figure 8. (a) Chondrite-normalized REE patterns; (b) and Primitive Mantle (PM) normalized trace element diagrams for the amphibolites, metagabbros. Chondrite, PM values are from [42] and OIB, E-MORB and NMORB values are from [43].

6. Discussion

6.1. Magmatic Differentiation of the Meta-Mafic Rocks

In this study, we assess the extent of alteration, crustal contamination, and fractional crystallization affecting the meta-mafic rocks from the eastern part of the

Mayo Kebbi Massif (Pala). Geochemical data presented in **Table 1**, indicate that both amphibolites and metagabbros are generally characterized by low loss on ignition (LOI) values (<2.4%), suggesting minimal alteration, with the exception of one highly altered amphibolite sample (LOI = 10.4%). During alteration and metamorphism, major elements such as Na, K, and Ca, along with large-ion lithophile elements (LILEs) including Cs, Rb, Ba, Sr, and Pb, may become mobile. In contrast, elements such as Al_2O_3, TiO_2, high field strength elements (HFSEs), rare earth elements (REEs, except Ce and Eu), Th, and transition metals tend to remain immobile and are less sensitive to hydrothermal alteration. The use of these immobile elements and their ratios provides valuable insights into primary petrogenetic processes [44].

Amphibolites and metagabbros exhibit high Mg-number values (Mg# = 61 - 77), and are depleted in HFSEs (Zr, Hf, Nb, Ta) relative to REEs and LILEs (**Table 1**). These geochemical features are indicative of a primary mantle source [45], although they may also reflect crustal contamination [46]. However, the very low P_2O_5 contents ($0.01 < P_2O_5 < 0.15$) and negative P anomalies do not support significant crustal contamination. This interpretation is further supported by the Th/Yb vs Ta/Yb diagram, in which amphibolites and metagabbros show no trend toward sedimentary contamination. Major element diagrams (Al_2O_3, TiO_2, Fe_2O_3, MgO, CaO, Na_2O, and SiO_2) and trace element plots (V, Co, Ni, Cr, Ba, Y, Zr, and Ni) versus MgO reveal trends consistent with fractional crystallization, suggesting the removal of olivine, pyroxene, and plagioclase. This fractionation of olivine, clinopyroxene, and plagioclase is confirmed by the Sr versus Ba diagram [47] (**Figure 9**). Additionally, the parallelism of REE patterns and slight enrichment in LREEs further support the occurrence of fractional crystallization. The observed scatter in the TiO_2 and Nb versus MgO diagrams (**Figure 6** and **Figure 7**) may reflect crystal accumulation or dilution processes involving olivine and pyroxene, as well as minor hydrothermal alteration within the host rocks.

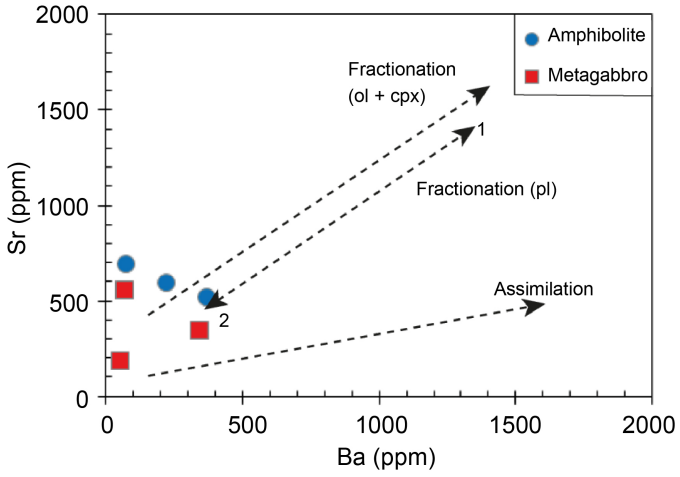

Figure 9. Illustration of olivine, clinopyroxène and plagioclase fractionation in the Sr versus Ba diagram of [47].

6.2. Magma Source

Geochemical data (**Table 1**) and the Zr versus MgO diagram [48] indicate that the amphibolites from the Pala region are of magmatic origin (**Figure 10(a)**). The suite of rocks, including amphibolite and metagabbro, originated from partial melting of basaltic protoliths, followed by metamorphic overprinting, as evidenced by the CaO/(MgO + FeOt) versus Al_2O_3/(MgO + FeOt) discrimination diagram presented by [49] (**Figure 10(b)**). This interpretation is consistent with the classification diagram of [39], in which all amphibolite and metagabbro samples plot within the field corresponding to a basaltic protolith. Similar types of amphibolites have been described in the southern part of the Ouaddaï Massif, although they are characterized by a gabbroic protolith [24]. This suggests regional variability in the nature of the original magmatic source, while maintaining a broadly mafic character.

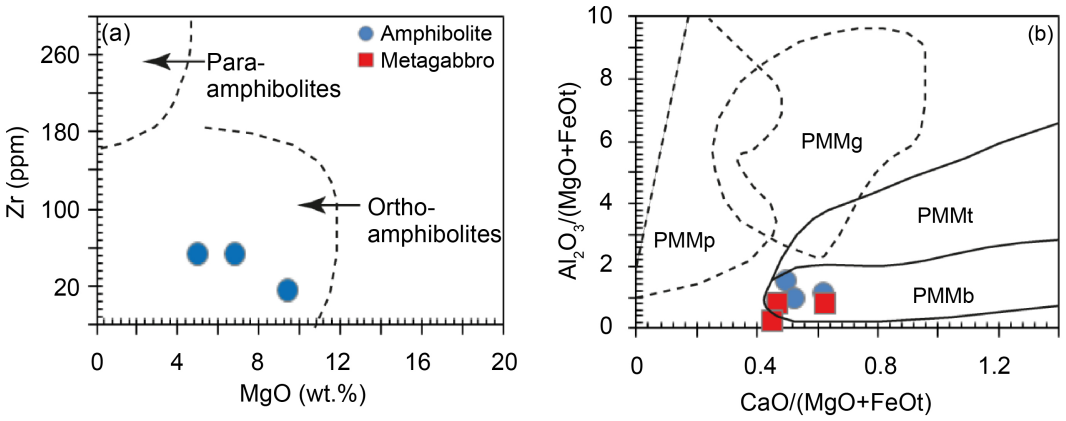

Figure 10. (a) Zr vs MgO [49] diagrams for the cumulate and massive pyroxene amphibolites. (b) Metagabbros in the Discrimination CaO/(MgO + FeOt) vs Al_2O_3/(MgO + FeOt) diagram of [50]. PMMg = Partial Melts from Metagreywackes; PMMp = Partial Melts from Metapelite; PMMt Partial Melts from Metatonalite and PPMb = Partial Melts from Metabasalte.

6.3. Tectonic Settings

Geochemical discrimination reveals the presence of both MORB-like and IAT-like components in the source of the amphibolites and metagabbros. In the V vs. TiO_2 diagram (**Figure 11(a)**), samples from the eastern Mayo Kebbi region predominantly plot within the MORB field, indicating a mid-ocean ridge basalt affinity. This interpretation is supported by the Hf/3-Th-Ta ternary diagram of [50] (**Figure 11(b)**), which shows a similar distribution. Further evidence is provided by the TiO_2/Yb vs. Nb/Yb [51] and Th/Yb vs. Nb/Yb diagram (**Figure 10(c)**, **Figure 10(d)**), where the samples cluster in the N-MORB field and near the depleted mantle domain. This geochemical trend is further evidenced by the depletion in incompatible elements such as Rb, Pb, Ba, and Sr, along with Zr/Nb ratios ranging from 15.91 to 34.62, values that fall within the typical range for normal MORB (Zr/Nb = 11 - 39). Negative anomalies in Nb-Ta, Zr-Hf and Ti, combined with Ba

and Sr enrichment in selected samples, reflect geochemical features characteristic of interoceanic tholeiitic arc basalts associated with subduction processes [52] [53]. The coexistence of MORB-like and arc-like geochemical signatures can be interpreted as the result of slab rollback, a process that induces extension in the overriding plate and promotes the upwelling of depleted mantle, generating MORB-type magmas. Simultaneously, the influence of subduction, derived fluids contributes to the formation of arc-type magmas. Such rock types have also been documented in the metabasalts of Mahakoshal Belt and the Sonakhan Greenstone Belt within the Central Indian Shield [54]. Moreover, Th/Ce ratios below 0.1 across all samples indicate negligible input from subducted sediments, in line with the findings of [55].

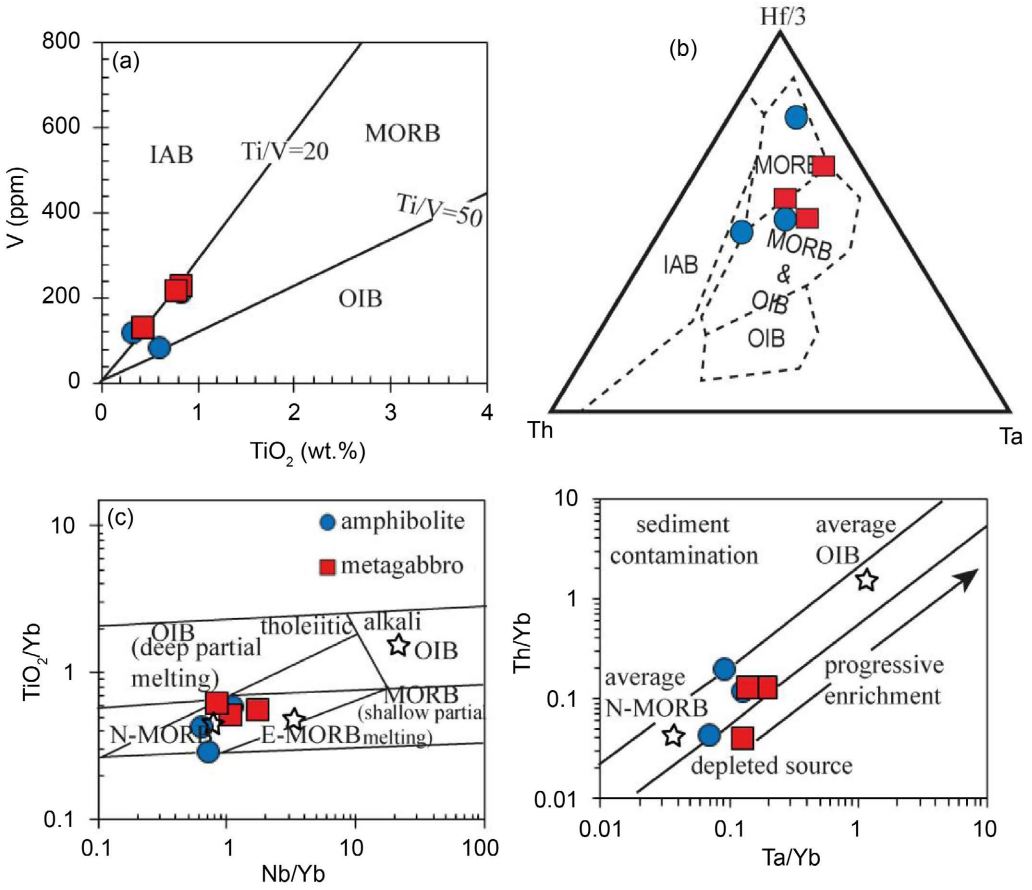

Figure 11. chemical tectonic environment discrimination diagrams of amphibolite and metagabbro of Pala: (a) V vs TiO_2; (b) Hf/3-Th-Ta diagram after [50]; (c) and (d) TiO_2/Yb vs. Nb/Yb, (Th/Yb vs. Ta/Yb diagram [51], illustrating that the amphibolite and metagabbros result from depleted N-MORB source.

6.4. Implications for Regional Geology

Amphibolites and metagabbros are sparsely represented within the Central African Orogenic Belt (CAOB) in Chad. Amphibolites from the southern part of the Ouaddaï massif exhibit a gabbroic affinity and are interpreted to result from par-

tial melting of a depleted mantle source, as indicated by εNd values of +4.4 and +3.8 at 550 Ma [23] [24]. Similarly, metagabbros identified at the Gauthiot Falls in the Mayo Kebbi region are derived from an ultrabasic protolith formed by partial melting of depleted mantle, with εNd values ranging from +3 to +6 at 650 Ma [32]. The present study, based primarily on petrographic and geochemical analyses of amphibolites and metagabbros, demonstrates that these rocks share comparable characteristics with those previously documented in the Ouaddaï and Mayo Kebbi regions. These similarities suggest a shared geodynamic history involving depleted mantle sources and subduction-related magmatism across the southern and north-eastern parts of the CAOB in Chad.

7. Conclusions

Geochemical signatures indicate that the amphibolites and metagabbros from the eastern Mayo Kebbi massif (Pala area) exhibit a calc-alkaline to tholeiitic affinity. These rocks record a geodynamic evolution characterized by:

- A magmatic origin linked to partial melting of basalts;
- Geochemical features dominated by N-MORB signatures;
- Elemental anomalies and trace element ratios indicative of intra-oceanic subduction influence;
- A depleted mantle source with minimal sedimentary contribution.

These converging lines of evidence support a tectonic model involving an active margin setting, situated between a mid-ocean ridge and an intra-oceanic arc. This reflects the complex dynamics of an ancient oceanic domain undergoing closure or subduction.

Acknowledgements

This research forms part of the broader scientific investigations led by the first author. The authors gratefully acknowledge the administrative authorities of Pala for their invaluable support and for granting permission to conduct fieldwork in the region. Special thanks are extended to Mr. Che Stephene (Douala) for his indispensable technical assistance during the sample pulverization process. The authors also wish to express their sincere appreciation to the team at ALS Geochemistry, Loughrea (Ireland), whose expertise and commitment were instrumental in carrying out the geochemical analyses.

Conflicts of Interest

The authors declare that they have no known competing financial interests or personal relationships that could have appeared to influence the work reported in this paper.

References

[1] Jackson, N.J. and Ramsay, C.R. (1980) What Is the "Pan-African"? A Consensus Is

Needed. *Geology*, **8**, 210-211.
https://doi.org/10.1130/0091-7613(1980)8<210:witpac>2.0.co;2

[2] Bessoles, B. and Trompette, R. (1980) Géologie de l'Afrique. La chaine panafricaine "Zone mobile d'Afrique centrale", (partie sud) et zone soudanaise. *Mémoire BRGM*, *Orléans*, **92**, 394.

[3] Castaing, C., Feybesse, J.L., Thiéblemont, D., Triboulet, C. and Chèvremont, P. (1994) Palaeogeographical Reconstructions of the Pan-African/Brasiliano Orogen: Closure of an Oceanic Domain or Intracontinental Convergence between Major Blocks? *Precambrian Research*, **69**, 327-344. https://doi.org/10.1016/0301-9268(94)90095-7

[4] Abdelsalam, M.G., Liégeois, J. and Stern, R.J. (2002) The Saharan Metacraton. *Journal of African Earth Sciences*, **34**, 119-136.
https://doi.org/10.1016/s0899-5362(02)00013-1

[5] de Almeida, F.F.M., Hasui, Y., de Brito Neves, B.B. and Fuck, R.A. (1981) Brazilian Structural Provinces: An Introduction. *Earth-Science Reviews*, **17**, 1-29.
https://doi.org/10.1016/0012-8252(81)90003-9

[6] Brito Neves, B.B., Santos, E.J. and Van Schmus, W.R. (2000) Tectonic History of the Borborema Province, Northeastern Brazil. In: Cordani, U., Milani, E.J., Thomaz Filho, A. and Campos, D.A., Eds., *Tectonic Evolution of South America*, Instituto de Geociências, Universidade de São Paulo, 151-182.

[7] Lerouge, C., Cocherie, A., Toteu, S.F., Penaye, J., Milési, J., Tchameni, R., *et al.* (2006) Shrimp U-Pb Zircon Age Evidence for Paleoproterozoic Sedimentation and 2.05Ga Syntectonic Plutonism in the Nyong Group, South-Western Cameroon: Consequences for the Eburnean-Transamazonian Belt of NE Brazil and Central Africa. *Journal of African Earth Sciences*, **44**, 413-427.
https://doi.org/10.1016/j.jafrearsci.2005.11.010

[8] Ganade de Araujo, C.E., Weinberg, R.F. and Cordani, U.G. (2013) Extruding the Borborema Province (NE-Brazil): A Two-Stage Neoproterozoic Collision Process. *Terra Nova*, **26**, 157-168. https://doi.org/10.1111/ter.12084

[9] Lima, J.V.D., Guimarães, I.D.P., Neves, S.P., Basei, M.A.S., da Silva Filho, A.F. and Brainer, C.C.G. (2021) Post-collisional, High-Ba-Sr Teixeira Batholith Granites: Evidence for Recycling of Paleoproterozoic Crust in the Alto Pajeú Domain, Borborema Province—NE-Brazil. *Lithos*, **404**, Article ID: 106469.
https://doi.org/10.1016/j.lithos.2021.106469

[10] Ganade, C.E., Weinberg, R.F., Caxito, F.A., Lopes, L.B.L., Tesser, L.R. and Costa, I.S. (2021) Decratonization by Rifting Enables Orogenic Reworking and Transcurrent Dispersal of Old Terranes in NE Brazil. *Scientific Reports*, **11**, Article No. 5719.
https://doi.org/10.1038/s41598-021-84703-x

[11] Martins Lino, L., Quiroz-Valle, F.R., Stipp Basei, M.Â., Farias Vlach, S.R., Hueck, M., Willbold, M., *et al.* (2023) Petrogenesis and Tectonic Significance of Two Bimodal Volcanic Stages from the Ediacaran Campo Alegre-Corupá Basin (Brazil): Record of Metacratonization during the Consolidation of Western Gondwana. *Precambrian Research*, **385**, Article ID: 106950. https://doi.org/10.1016/j.precamres.2022.106950

[12] Ngako, V. (1999) Les déformations continentales panafricaines en Afrique Centrale: Résultat d'un poinçonnement de type himalayen. Master's Thesis, Université de Yaoundé I.

[13] Ngako, V., Affaton, P., Nnange, J.M. and Njanko, T. (2003) Pan-African Tectonic Evolution in Central and Southern Cameroon: Transpression and Transtension during Sinistral Shear Movements. *Journal of African Earth Sciences*, **36**, 207-214.

https://doi.org/10.1016/s0899-5362(03)00023-x

[14] Ferré, E.C., Caby, R., Peucat, J.J., Capdevila, R. and Monié, P. (1998) Pan-African, Post-Collisional, Ferro-Potassic Granite and Quartz-Monzonite Plutons of Eastern Nigeria. *Lithos*, **45**, 255-279. https://doi.org/10.1016/s0024-4937(98)00035-8

[15] Ferré, E., Gleizes, G. and Caby, R. (2002) Obliquely Convergent Tectonics and Granite Emplacement in the Trans-Saharan Belt of Eastern Nigeria: A Synthesis. *Precambrian Research*, **114**, 199-219. https://doi.org/10.1016/s0301-9268(01)00226-1

[16] Pegram, W.J., Register, J.K., Fullagar, P.D., Ghuma, M.A. and Rogers, J.J.W. (1976) Pan-African Ages from a Tibesti Massif Batholith, Southern Libya. *Earth and Planetary Science Letters*, **30**, 123-128. https://doi.org/10.1016/0012-821x(76)90014-5

[17] Suayah, I.B., Miller, J.S., Miller, B.V., Bayer, T.M. and Rogers, J.J.W. (2006) Tectonic Significance of Late Neoproterozoic Granites from the Tibesti Massif in Southern Libya Inferred from Sr and Nd Isotopes and U-Pb Zircon Data. *Journal of African Earth Sciences*, **44**, 561-570. https://doi.org/10.1016/j.jafrearsci.2005.11.020

[18] Wacrenier, P. (1958) Carte géologique provisoire du Borkou-Ennedi-Tibesti. DMG AEF.

[19] Wacrenier, P. and Vincent, P.M. (1958) Notice explicative de la carte géologique provisoire du Borkou-Ennedi-Tibesti Brazaville, Direction des Mines et de la Géologie.

[20] Kasser, M.Y. (1995) Evolution précambrienne de la région du Mayo Kebbi (Tchad). Un segment de la Chaîne Panafricaine. Master's Thesis, Muséum d'Histoire Naturelle de Paris (France).

[21] Liégeois, J.P. (1993) Mesures des isotopes du Sr en vue de détermination d'âges des roches magmatiques du Centre du Tchad (région du Ouaddaï). Muséum Royal d'Afrique Centrale (Belgique).

[22] Djerossem, N.F. (2018) Croissance et remobilisation crustales au Pan-Africain dans le Sud du massif du Ouaddaï au Tchad. Master's Thesis, Université Paul Sabatier de Toulouse (France).

[23] Djerossem, F., Berger, J., Vanderhaeghe, O., Isseini, M., Ganne, J. and Zeh, A. (2020) Neoproterozoic Magmatic Evolution of the Southern Ouaddaï Massif (Chad). *BSGF—Earth Sciences Bulletin*, **191**, 34. https://doi.org/10.1051/bsgf/2020032

[24] Djerossem, F., Zeh, A., Isseini, M., Vanderhaeghe, O., Berger, J. and Ganne, J. (2021) U-Pb-Hf Isotopic Systematics of Zircons from Granites and Metasediments of Southern Ouaddaï (Chad), Implications for Crustal Evolution and Provenance in the Central Africa Orogenic Belt. *Precambrian Research*, **361**, Article ID: 106233. https://doi.org/10.1016/j.precamres.2021.106233

[25] Djerossem, F.N., Mbassa, B.J., Vanderhaeghe, O. and Gregoire, M. (2024) The Iriba Alkaline Basalts, an Expression of Mantle-Derived Cretaceous Magmatism of the Cameroon-Chad Volcanic Line along the Central Africa Rift System. *Comptes Rendus. Géoscience*, **356**, 231-248. https://doi.org/10.5802/crgeos.282

[26] de Wit, M.J., Bowring, S., Buchwaldt, R., Dudas, F.Ö., MacPhee, D., Tagne-Kamga, G., *et al.* (2021) Geochemical Reconnaissance of the Guéra and Ouaddaï Massifs in Chad: Evolution of Proterozoic Crust in the Central Sahara Shield. *South African Journal of Geology*, **124**, 353-382. https://doi.org/10.25131/sajg.124.0048

[27] Shellnutt, J.G., Denyszyn, S.W. and Pang, K. (2021) Editorial: Granite Petrogenesis and Geodynamics. *Frontiers in Earth Science*, **8**, Article 637729. https://doi.org/10.3389/feart.2020.637729

[28] Liégeois, J.P. (1992) Mesures des isotopes du Sr en vue de détermination d'âges des roches magmatiques du Centre du Tchad (régions de Baïbokoum, Léré-Figuil).

[29] Kusnir, I. and Moutaye, H.A. (1997) Ressources minérales du Tchad: Une revue. *Journal of African Earth Sciences*, **24**, 549-562. https://doi.org/10.1016/s0899-5362(97)00080-8

[30] Baïssemia Ronang, G., Gountié Dedzo, M., Tcheumenak Kouémo, J., Klamadji, M.N., Mbaguedjé, D. and Kwékam, M. (2024) Petrography and Geochemical Characterization of the Baïbokoum Syenitic Pluton (Southern Chad): Implication for the Magma Genesis. *Acta Geochimica*, **44**, 420-439. https://doi.org/10.1007/s11631-024-00733-y

[31] Doumnang, J.C. (2006) Géologie des formations Néoprotérozoïques du Mayo-Kebbi (Sud-Ouest du Tchad), Apports de la pétrologie et de la géochimie, implications sur la géodynamique au Pan-Africain. Master's Thesis, Université d'Orléans (France).

[32] Isseini, M. (2011) Croissance et différenciation crustales au Néoprotérozoïque: Exemple du domaine panafricain du Mayo-Kebbi au Sud-Ouest du Tchad. Master's Thesis, Université Henri Poincaré.

[33] Isseini, M., André-Mayer, A., Vanderhaeghe, O., Barbey, P. and Deloule, E. (2012) A-type Granites from the Pan-African Orogenic Belt in South-Western Chad Constrained Using Geochemistry, Sr-Nd Isotopes and U-Pb Geochronology. *Lithos*, **153**, 39-52. https://doi.org/10.1016/j.lithos.2012.07.014

[34] Penaye, J., Kröner, A., Toteu, S.F., Van Schmus, W.R. and Doumnang, J. (2006) Evolution of the Mayo Kebbi Region as Revealed by Zircon Dating: An Early (ca. 740ma) Pan-African Magmatic Arc in Southwestern Chad. *Journal of African Earth Sciences*, **44**, 530-542. https://doi.org/10.1016/j.jafrearsci.2005.11.018

[35] Mbagdje, D. (2015) Métallogénie de l'or et de l'uranium dans le cadre de la croissance et de la différenciation de la croûte au Néoprotérozoïque: Exemple du massif du Mayo-Kebbi (Tchad) dans la Ceinture Orogénique d'Afrique Centrale. Master's Thesis, Université de Lorraine.

[36] Olivier, V., André-Mayer, A., Diondoh, M., Aurélien, E., Maryse, O., Moussa, I., *et al.* (2020) Uranium Mineralization Associated with Late Magmatic Ductile to Brittle Deformation and Na-Ca Metasomatism of the Pan-African A-Type Zabili Syntectonic Pluton (Mayo-Kebbi Massif, SW Chad). *Mineralium Deposita*, **56**, 1297-1319. https://doi.org/10.1007/s00126-020-00999-1

[37] Pouclet, A., Vidal, M., Doumnang, J., Vicat, J. and Tchameni, R. (2006) Neoproterozoic Crustal Evolution in Southern Chad: Pan-African Ocean Basin Closing, Arc Accretion and Late- to Post-Orogenic Granitic Intrusion. *Journal of African Earth Sciences*, **44**, 543-560. https://doi.org/10.1016/j.jafrearsci.2005.11.019

[38] Bas, M.J.L., Maitre, R.W.L., Streckeisen, A. and Zanettin, B. (1986) A Chemical Classification of Volcanic Rocks Based on the Total Alkali-Silica Diagram. *Journal of Petrology*, **27**, 745-750. https://doi.org/10.1093/petrology/27.3.745

[39] Pearce, J.A. (1996) A Users Guide to Basalt Discrimination Diagrams. In: Wyman, D., Ed., *Trace Element Geochemistry of Volcanic Rocks*: *Application for Massive Sulphide Exploration*, Geological Association of Canada, 79-113.

[40] Irvine, T.N. and Baragar, W.R.A. (1971) A Guide to the Chemical Classification of the Common Volcanic Rocks. *Canadian Journal of Earth Sciences*, **8**, 523-548. https://doi.org/10.1139/e71-055

[41] Pearce, J.A. and Cann, J.R. (1971) Ophiolite Origin Investigated by Discriminant Analysis Using Ti, Zr and Y. *Earth and Planetary Science Letters*, **12**, 339-349.

https://doi.org/10.1016/0012-821x(71)90220-2

[42] McLennan, S.M. (1989) Chapter 7. Rare Earth Elements in Sedimentary Rocks: Influence of Provenance and Sedimentary Processes. In: Lipin, B.R. and MacKay, G.A., Eds., *Geochemistry and Mineralogy of Rare Earth Elements*, De Gruyter, 169-200. https://doi.org/10.1515/9781501509032-010

[43] McDonough, W.F. and Sun, S. (1995) The Composition of the Earth. *Chemical Geology*, **120**, 223-253. https://doi.org/10.1016/0009-2541(94)00140-4

[44] Said, N., Kerrich, R. and Groves, D. (2010) Geochemical Systematics of Basalts of the Lower Basalt Unit, 2.7Ga Kambalda Sequence, Yilgarn Craton, Australia: Plume Impingement at a Rifted Craton Margin. *Lithos*, **115**, 82-100. https://doi.org/10.1016/j.lithos.2009.11.008

[45] Frey, F.A., Green, D.H. and Roy, S.D. (1978) Integrated Models of Basalt Petrogenesis: A Study of Quartz Tholeiites to Olivine Melilitites from South Eastern Australia Utilizing Geochemical and Experimental Petrological Data. *Journal of Petrology*, **19**, 463-513. https://doi.org/10.1093/petrology/19.3.463

[46] Polat, A., Appel, P.W.U., Fryer, B., Windley, B., Frei, R., Samson, I.M., *et al.* (2009) Trace Element Systematics of the Neoarchean Fiskenæsset Anorthosite Complex and Associated Meta-Volcanic Rocks, SW Greenland: Evidence for a Magmatic Arc Origin. *Precambrian Research*, **175**, 87-115. https://doi.org/10.1016/j.precamres.2009.09.002

[47] Franz, G., Steiner, G., Volker, F., Pudlo, D. and Hammerschmidt, K. (1999) Plume Related Alkaline Magmatism in Central Africa—The Meidob Hills (W Sudan). *Chemical Geology*, **157**, 27-47. https://doi.org/10.1016/s0009-2541(98)00195-8

[48] Geringer, G.J. (1979) The Origin and Tectonic Setting of Amphibolites in Part of Namaqua Metamorphic Belt, South Africa, Traa. *Geological Society of South Africa*, **82**, 287-303.

[49] Gerdes, A., Montero, P., Bea, F., Fershater, G., Borodina, N., Osipova, T., *et al.* (2001) Peraluminous Granites Frequently with Mantle-Like Isotope Compositions: The Continental-Type Murzinka and Dzhabyk Batholiths of the Eastern Urals. *International Journal of Earth Sciences*, **91**, 3-19. https://doi.org/10.1007/s005310100195

[50] Wood, D.A. (1980) The Application of a Thhfta Diagram to Problems of Tectonomagmatic Classification and to Establishing the Nature of Crustal Contamination of Basaltic Lavas of the British Tertiary Volcanic Province. *Earth and Planetary Science Letters*, **50**, 11-30. https://doi.org/10.1016/0012-821x(80)90116-8

[51] Pearce, J.A. (2014) Immobile Element Fingerprinting of Ophiolites. *Elements*, **10**, 101-108. https://doi.org/10.2113/gselements.10.2.101

[52] Kelemen, P.B., Kikawa, E., Miller, D.J. and Ship-Board Science Party (2004) Proceedings of the Ocean Drilling Program, Initial Reports, Vol-29: College Station, Texas, Ocean Drilling Program. https://doi.org/10.2973/odp.proc.ir.209.2004

[53] Pearce, J.A. (2008) Geochemical Fingerprinting of Oceanic Basalts with Applications to Ophiolite Classification and the Search for Archean Oceanic Crust. *Lithos*, **100**, 14-48. https://doi.org/10.1016/j.lithos.2007.06.016

[54] Wani, H. and Mondal, M.E.A. (2018) Geochemistry and Tectonic Setting of the Precambrian Mahakoshal and Sonakhan Greenstone Belts of the Central Indian Shield. In: Mondal, M., Ed., *Geological Evolution of the Precambrian Indian Shield*, Springer, 695-724. https://doi.org/10.1007/978-3-319-89698-4_26

[55] Hawkesworth, C.J., Turner, S.P., McDermott, F., Peate, D.W. and van Calsteren, P.

(1997) U-Th Isotopes in Arc Magmas: Implications for Element Transfer from the Subducted Crust. *Science*, **276**, 551-555.
https://doi.org/10.1126/science.276.5312.551